Journal of Alloys and Compounds 857 (2021) 157991

Contents lists available at ScienceDirect

Journal of Alloys and Compounds

journal homepage: http://www.elsevier.com/locate/jalcom

FeSiBCrC amorphous magnetic powder fabricated by gas-water combined atomization

Tongchun Zhao [a, 1], Cunguang Chen [a, b, **, 1], XiaoJie Wu [a], Chenzeng Zhang [a], Alex A. Volinsky [c], Junjie Hao [a, b, *]

[a] Institute for Advanced Materials and Technology, University of Science and Technology Beijing, Beijing, 100083, PR China
[b] Innovation Group of Marine Engineering Materials and Corrosion Control, Southern Marine Science and Engineering Guangdong Laboratory (Zhuhai), Zhuhai, 519000, PR China
[c] Department of Mechanical Engineering, University of South Florida, Tampa, FL, 33620, USA

ARTICLE INFO

Article history:
Received 12 August 2020
Received in revised form
12 November 2020
Accepted 16 November 2020
Available online 20 November 2020

Keywords:
Amorphous powder
Gas-water combined atomization
Soft magnetic composites

ABSTRACT

Amorphous soft magnetic composites have been attracting attention because of its low core loss under high frequency application. It is demanded that the powder for fabricating amorphous soft magnetic composites has amorphous structure and nearly spherical shape, which facilitates the uniform coating of insulator on the surface of powder particles. In this paper, amorphous $Fe_{73.5}Si_{13}B_{11}Cr_1C_{1.5}$ (at%) powder was produced by gas-water combined atomization process which takes advantages of both gas atomization and water atomization, and its properties was compared with powder produced by gas atomization and water atomization. Gas-water combined atomization powder with particle size of −60 μm were found to be amorphous with low coercivity, and the shape of particles was nearly spherical. The permeability of magnetic powder cores prepared with three kinds of powder first increased and then decreased with annealing temperature, and the core loss first decreased and then increased. The cores prepared with gas-water combined atomization powder showed the best overall properties, with an effective permeability of 26.9, a relative permeability of 83.3% under a superimposed DC magnetic field of 7.96 kA/m, a core loss of 258 mW/cm^3 under a frequency of 100 kHz, and a magnetization intensity B_m of 0.05 T after annealing at 793 K in nitrogen gas.

1. Introduction

Soft magnetic composites (SMCs) formed from ferromagnetic powder after insulation treatment are widely used in communications, electronics, switching power supplies and other applications because of their high saturation magnetic induction intensity, stable permeability and low energy loss [1–4]. With increasing demand for electronic devices with the high-frequency operation, small size, large power output and high energy efficiency, the performance requirements for SMCs are becoming more stringent. Researchers and end users have focused on amorphous SMCs because of their low coercivity and high resistivity [5–7], which enable amorphous SMCs to operate under high frequency of 1.5–3 GHz [8].

The permeability, core loss and DC bias performance of SMCs are closely related to the chemical composition, particle size and shape of powders [9–13]. A smooth surface and spherical shape of particles are beneficial for insulation coatings, which can decrease the eddy current between particles and accordingly reduce loss. In addition, the degree of internal crystallization in amorphous powder also affects the permeability and coercivity. Abnormal crystallization and precipitation of the secondary phases increase the coercivity and degrades the soft magnetic properties of the material [14–16]. Therefore, an appropriate amorphous phase content and nearly spherical particles without sharp protrusion are prerequisites for obtaining amorphous SMCs with high performance.

Amorphous powder is usually prepared by strip crushing, mechanical alloying or atomization. In the strip crushing process, a metal melt flows through a slit nozzle onto a high-speed rotating

* Corresponding author. Institute for Advanced Materials and Technology, University of Science and Technology Beijing, Beijing, 100083, PR China.
** Corresponding author. Institute for Advanced Materials and Technology, University of Science and Technology Beijing, Beijing, 100083, PR China.
E-mail addresses: cgchen@ustb.edu.cn (C. Chen), haojunjie@ustb.edu.cn (J. Hao).
[1] These authors contributed equally to this work.

https://doi.org/10.1016/j.jallcom.2020.157991
0925-8388/

copper roll, rapidly solidifying into an amorphous strip of 20–30 μm thick, and then the strip is mechanically crushed and ball-milled to produce powder [17–20]. For mechanical alloying, pure metal or metalloid materials are cold welded and diffused into each other to fabricate amorphous powder by high-energy ball milling [21–23]. The powders prepared by these two methods have irregular shapes with sharp protrusions and corners, which is not conducive to powder insulation coating. When the soft magnetic composites are pressed and formed, the insulating layer can be easily pierced, which tends to increase the core loss. Moreover, the different arrangement of flake powder would lead to the anisotropy of magnetic properties of the powder cores [24]. In gas atomization (GA) or water atomization (WA) processes, molten metal liquid is broken up with a high-pressure inert gas or high-pressure water jet, and then the resulting droplets are cooled and solidified into powder. The cooling rates of melt droplets in GA and WA are approximately 10^2–10^3 K/s and 10^3–10^4 K/s, respectively [25]. GA powders have a nearly spherical shape, but the low cooling rate is not conducive to amorphous structure formation [26,27]. The higher cooling rate of WA is conducive to amorphous structure formation, but the powder contains some irregular particles and coarse surfaces, which again is not beneficial to powder insulation coating [28,29]. Otsuka et al. prepared Fe(Si)BC amorphous powder by the spinning water atomization process (SWAP) [30], in which metal liquid is first broken up by a nitrogen jet and the resulting droplets fall into high-speed rotating water flow. As a result, nearly spherical powder was obtained at a 10^6 K/s cooling rate. This process offers significant progress for preparation amorphous powder. However, it requires accurate coordination of the gas nozzle and rotating water, and the realization of a high-speed water flow is difficult. Aiming to increase cooling rate of gas atomization for preparing soft ferromagnetic amorphous powder, Ciftci et al. developed two strategies [31]. On the one hand, four dual argon/water nozzles were arranged below gas atomizer, operated with a water flow of 400 mL/min and an argon pressure of 0.55 MPa. Molten metal droplets initially generated by gas atomizer were cooled by the spry cone of water and argon mixture. On the other hand, molten metal droplets fell into water directly in the vessel below gas atomizer. In spite of increasing the cooling rate through both methods, the cooling rate was still relatively low for the small water flux in the first method and a far distance from the surface of water in the vessel to gas atomizer in the second method.

A variety of soft magnetic amorphous alloys have been developed on the basis of Fe–Si–B composition system in recent years. Adding C into Fe–Si–B can greatly improve glass forming ability (GFA) of the alloy, with high saturation magnetic induction intensity (B_s) [32]. The addition of Cr into Fe–Si–B–C and similar alloys can increase the resistivity and corrosion resistance [33,34]. Magnetic powder cores prepared by powder treated by nitric acid has low loss [35]. By means of sol-gel method, flaky FeSiBCCr magnetic powders were coated with inorganic (SiO_2) insulating layer, and the DC bias and core loss of powder cores were both improved [36]. The Fe–Si–B–Cr–C powder has been used to manufacture SMCs used in laptops, mobile phones and other high frequency (>1 MHz) communication equipment. In order to further reduce the loss of SMC and increase the corrosion resistance, $Fe_{73.5}Si_{13}B_{11}Cr_1C_{1.5}$ (at%) alloy powder was studied in this paper.

To obtain spherical amorphous powder, in this work, we prepared $Fe_{73.5}Si_{13}B_{11}Cr_1C_{1.5}$ (at%) amorphous powder using combined gas-water atomization (CA) technology, pressed and formed toroidal magnetic powder cores, and conducted comparisons with GA powder and WA powder with the same particle size and composition to determine the differences among their properties and evaluate the possibility of fabricating powder for soft magnetic composites by CA.

2. Experiment

Three kinds of atomization processes are schematically shown in Fig. 1. The melt liquid flows down through a delivery tube at the bottom of a tundish. As shown in Fig. 1a and b, the downward-flowing melt liquid is broken up by a high-pressure water jet or gas jet during the WA and GA processes. Alternatively, the melt liquid is broken up in two steps, i.e., first by a high-pressure gas jet and then by a low-pressure water jet, and further cooled by the water jet during the CA process, as shown in Fig. 1c. The structure and process parameters of the CA system are optimized so that after the metal liquid is broken up by the nitrogen jet, when spheroidization of the droplets has completed but the droplets have not yet solidified, most droplets are cooled by water, and only a small number of large droplets are further broken up by the water.

An alloy with an atomic ratio of $Fe_{73.5}Si_{13}B_{11}Cr_1C_{1.5}$ (at%) was characterized using the mass ratio of each element, and the burn loss of each element was estimated during smelting. A total mass of 50 kg of pure iron, pure silicon, boron iron alloy (the boron content was 18.3 wt%), pure chromium and pure graphite were loaded into a corundum crucible in a medium-frequency induction vacuum furnace. The materials were melted until the temperature of the metal liquid rose to 1693 K. After maintaining at this temperature for 5 min, the metal liquid was poured into the tundish and flowed through a delivery tube with a 5 mm inner diameter, immediately broken up by a high-pressure nitrogen gas jet and then solidified into powder. The water pressure was 50 MPa for WA with a water flow of 125 L/min, and the nitrogen pressure was 4.5 MPa for GA. For CA, the nitrogen pressure was 4.5 MPa and water pressure was 1.5 MPa with 125 L/min water flow. The collected powder was dried in a double-cone vacuum dryer with a 300 L volume. To eliminate the impact of the particle size on the properties of the powder and soft magnetic composites, the dried powder was screened to $-60 + 45$ μm, $-45 + 38$ μm, and -38 μm interval sizes, and each interval powder was taken as 5 wt%, 20 wt%, and 75% wt and blended in a V-shaped blender for 1 h to ensure each powder sample has the similar particle size distribution. The median diameter D50 and the oxygen content of the blended powder are listed in Table 1.

Three kinds of -60 μm powder were annealed at 693 K, 743 K, 793 K, or 843 K in a resistance wire heating tubular furnace with nitrogen protection for 1 h, and then the crystallization behavior of the powder was analyzed. Unannealed powder was passivated in 1 wt% phosphoric acid water solution containing 0.5 wt% acetone for 30 min, and then the passivated powder was vacuum dried at 373 K. 1.5 wt% silicone resin as an insulating agent and 0.5 wt% zinc stearate as a lubricant were added to the dried powder and evenly mixed for 30 min. Toroidal soft magnetic composites (also referred to as magnetic powder cores) with an outer diameter of 14 mm, an inner diameter of 8 mm, and a height of 3.6 mm were fabricated by unidirectional cold pressing under a pressure of 1600 MPa at room temperature. The compacted cores were annealed at 423 K, 693 K, 743 K, 793 K, and 843 K for 1 h in nitrogen and then cooled to room temperature in the oven.

The internal structural characteristics of the powder were analyzed by X-ray diffraction (XRD, Bruker D8 Discover), and the morphology of the powder was observed by a scanning electron microscope (SEM, FEI Nova nanoSEM450). Bright-field images were obtained with selected area electron diffraction (SAED) using a transmission electron microscope (TEM, FEI Talos F200). Endothermic and exothermic reactions of the powder during heating were measured by differential scanning calorimetry (DSC, Netzsch DSC404) in an argon atmosphere with the flow rate of 50 mL/min. The particle size of the powder was measured by a laser particle size meter (Malvern Mastersizer 2000), and the saturation

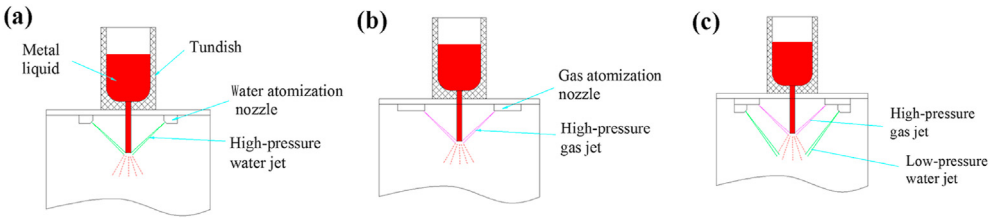

Fig. 1. Schematics of the three atomization methods: (a) Water atomization, (b) Gas atomization and (c) Gas-water combined atomization.

Table 1
Median size and oxygen content of powder for fabricating magnetic powder cores.

Powder	Median size D50 (μm)	Oxygen content (wt%)
WA powder	26.1 ± 0.2	0.087 ± 0.001
GA powder	25.6 ± 0.2	0.012 ± 0.001
CA powder	25.2 ± 0.2	0.059 ± 0.001

polarization magnetization (J_s) and coercivity (H_c) were measured at room temperature with a vibrating sample magnetometer (VSM, LakeShore 741) under a maximum applied field of 796 kA/m. The core loss of the magnetic powder cores was measured by a B–H analyzer (IWATSU-SY-8232) under different frequencies of 10 kHz, 50 kHz, 100 kHz, 150 kHz, and 200 kHz with B_m of 0.05 T. The effective permeability (μ_e) and DC bias performance were measured by an LCR meter (Agilent E4980A) under 1 V and 100 kHz frequency with 30 turns of copper wire of 0.35 mm diameter twisted on powder cores. The effective permeability was calculated as:

$$\mu_e = \frac{L.l_e}{\mu_0 N^2 .A_e} \quad (1)$$

Here, μ_e is the effective permeability, L is the inductance of magnetic powder cores measured by the LCR meter, l_e is the effective magnetic circuit length of magnetic powder cores, N is the number of copper wires turns (30 in this measurement) twisted on the surface of magnetic powder cores, A_e is the effective cross-sectional area of magnetic powder cores, and μ_0 is the permeability of vacuum ($4\pi \times 10^{-7}$ H/m).

3. Results and discussion

3.1. Powder properties

Fig. 2 shows the SEM morphology of the WA, GA, and CA $Fe_{73.5}Si_{13}B_{11}Cr_1C_{1.5}$ (at%) powder with the size of −60 μm. Some WA powder particles have long rod shape and sharp protrusions on the surface, as seen in Fig. 2a. During the WA proc$\mu_e = \frac{L \cdot l_e}{\mu_0 N^2 \cdot A_e}$ess, owing to the high cooling rate, the solidification time of the metal droplets was shorter than the spheroidization time, and spheroidization of some particles had not completed before solidification. During the GA process, the solidification time of the metal droplets was longer than that of spheroidization, and spheroidization had completed before solidification, so most particles are spherical as seen in Fig. 2b. On the other hand, because of the lower cooling rate, some flying melt droplets collided with solidified particles and ultimately covered the surface of those particles, leading to a coarse surface. Fig. 2c shows that nearly all CA powder has a spherical shape, with the best sphericity among the three kinds of powder. Relevant research has determined that after a metal liquid is broken up by a gas or water jet during the atomization process, the subsequent solidification process is related to the temperature of the droplets, cooling medium, viscosity and surface tension of the liquid metal. Under the action of the surface tension, the powder tends to spheroidize, and the shape of the powder is determined by the spheroidization time and solidification time [37–39]. If the solidification time of the metal droplets is longer than the spheroidization time or the difference between both is not significant, spheroidization completes before solidification. Under this condition, the powder particles generally have spherical shape. Otherwise, the surfaces of the powder particles are rough, and their shapes are irregular.

Fig. 3 shows the XRD patterns of the three kinds of powder with different particle sizes. A small sharp peak is present on the base of the broad diffuse halo at approximately 45° diffraction angle (2θ) in the XRD patterns for all the −150 + 105 μm powder, which is more obvious for the gas powder. These results indicate that the powder is mostly amorphous but partially crystallized. No sharp peaks present in the pattern of the −105 + 60 μm WA and GA powder, whose XRD patterns show only a broad diffuse halo, but a small sharp peak still exists in the XRD pattern of the −105 + 60 μm GA powder. In addition, only a broad diffuse halo and no sharp peak appears in the XRD pattern of all three kinds of the −60 μm powder. Under the same particle size interval, amorphous structure formation in the GA powder is more difficult than in the WA and CA powder, which verifies that GA has a lower cooling rate than WA and CA, but WA and CA have similar cooling rates. Owing to the amorphous structure formed in coarse powder and the spherical shape, CA has advantages over both WA and GA.

Figs. 4–6 show TEM bright field images, SAED results and the high-resolution images of the −60 μm WA, CA and GA powder, respectively. For the WA and CA powders, the bright field images are very similar and homogeneous, and no grains or other phases have precipitated. Only diffuse haloes are present in the SAED image, and a disorder lattice arrangement is shown in the high-resolution image. All TEM results indicate that the WA and CA powders are almost amorphous, which is consistent with the XRD patterns. In contrast, the TEM results of the GA powder exhibit obvious differences from the other two powders. Many fine grains below the 5 nm size are embedded unevenly in the amorphous matrix as seen in Fig. 6a. Discontinuous bright rings with spots located on their periphery appear in the SAED image, which indicates that many grains exist in the powder and that these grains have a preferred orientation. The precipitated grains are identified as the α-Fe(Si) phase. As seen in Fig. 6c, the crystal lattice has a periodically regular arrangement, and the lattice plane distance is approximately 0.204 nm. A fast Fourier transform (FFT) was performed in the red rectangle area, revealing bright spots presenting the α-Fe(Si) lattice plane, indicating a single crystal. Though nanoscale grains precipitated in the amorphous matrix, their very fine size caused diffraction peak broadening so that no sharp peaks appear. From the TEM results, the reason for crystallization in the GA powder is that the cooling rate of GA is lower than WA and CA.

DSC curves of the three kinds of powder with the particle size of −60 μm are shown in Fig. 7, and no glass transition temperature

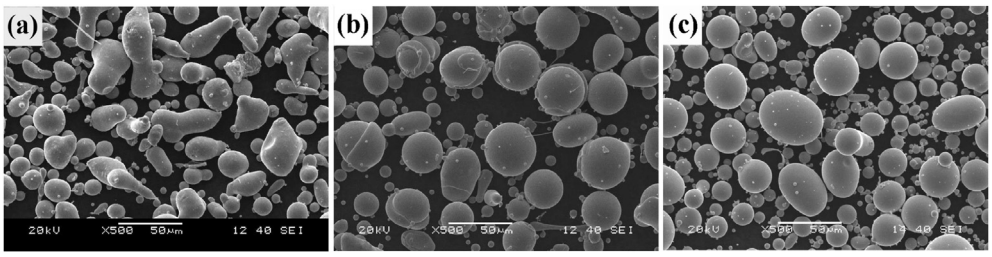

Fig. 2. SEM morphology of the $Fe_{73.5}Si_{13}B_{11}Cr_1C_{1.5}$ powder with −60 μm particle size: (a) WA, (b) GA and (c) CA.

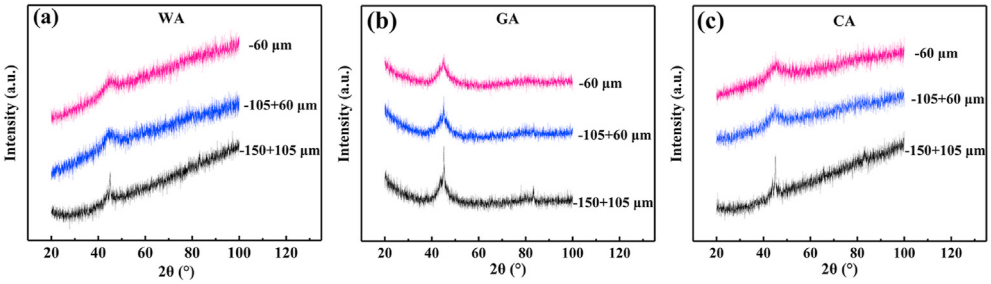

Fig. 3. XRD patterns of the $Fe_{73.5}Si_{13}B_{11}Cr_1C_{1.5}$ powder with different particle size: (a) WA, (b) GA and (c) CA.

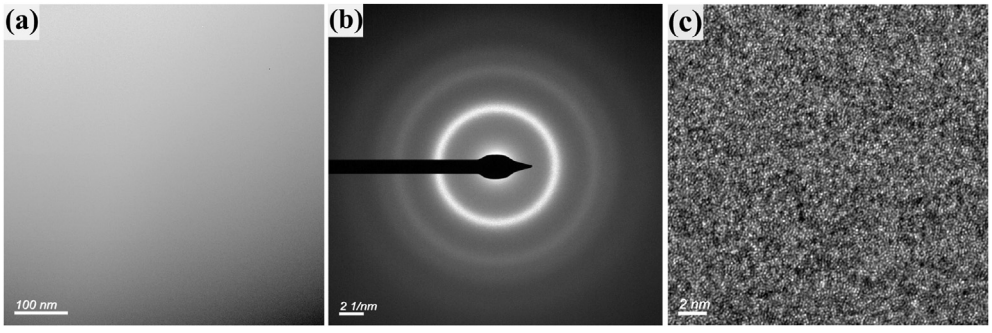

Fig. 4. TEM pattern of the $Fe_{73.5}Si_{13}B_{11}Cr_1C_{1.5}$ WA powder with −60 μm particle size: (a) Bright field image (b) SAED pattern and (c) High-resolution image.

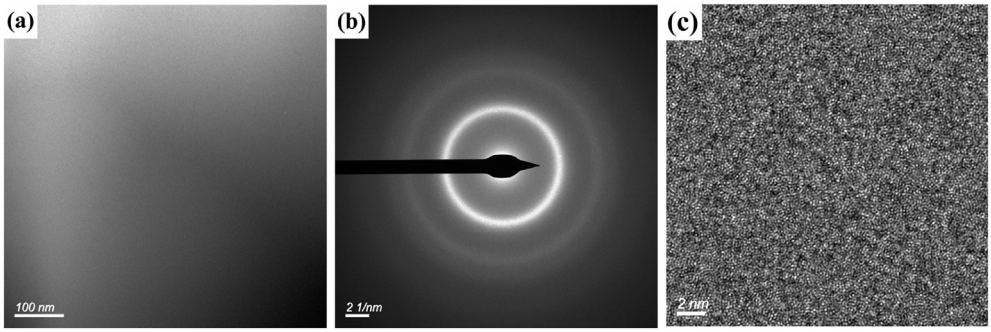

Fig. 5. TEM pattern of the $Fe_{73.5}Si_{13}B_{11}Cr_1C_{1.5}$ CA powder with −60 μm particle size: (a) Bright field image (b) SAED pattern and (c) High-resolution image.

T_g can be identified. The first crystallization onset temperature T_{x1} and first peak temperature T_{p1} of each powder are listed in Table 2. T_{x1} and T_{p1} are respectively 817.7 K and 826.9 K for the GA powder, 820.9 K and 826.4 K for the WA powder, and 824.3 K and 831.0 K for the CA powder. Since nanograins precipitated in the GA powder before heating, thus supplying nucleation locations for crystallization, the driving force for crystallization decreased, and T_{x1} and T_{p1} are relatively low. Both the WA and CA powders are almost amorphous, but the cooling rate of the metal droplets during WA is higher than GA. The higher cooling rate results in more amorphization in the WA powder, resulting in higher energy for crystal transitions. Additionally, each DSC curve has a small second exothermic peak after the first exothermic peak, indicating that after the first crystallization, a second crystal phase arises with the

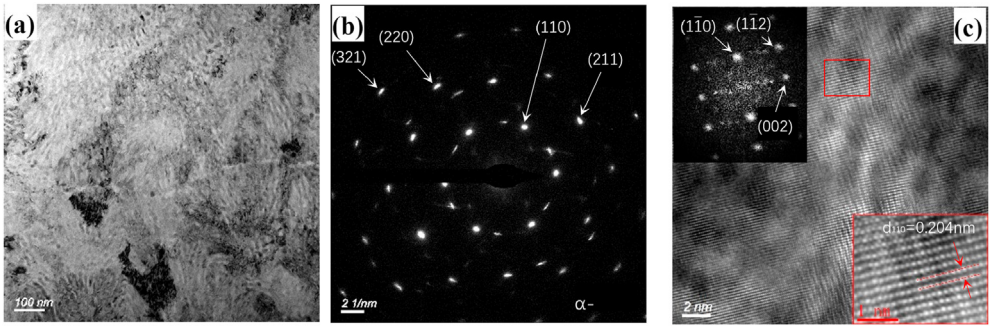

Fig. 6. TEM pattern of the $Fe_{73.5}Si_{13}B_{11}Cr_1C_{1.5}$ GA powder with −60 μm particle size: (a) Bright field image (b) SAED output and (c) High-resolution image and FFT of the selected area.

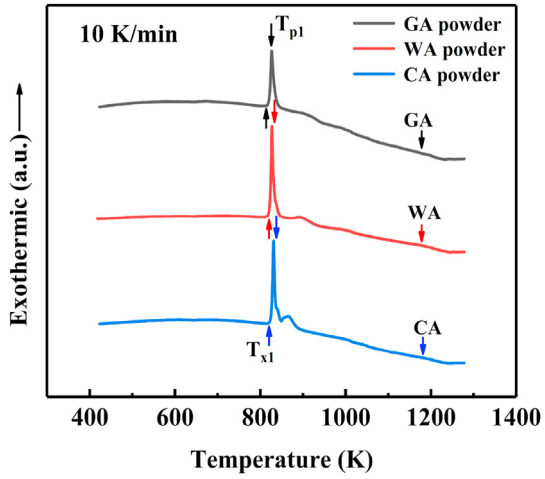

Fig. 7. DSC curves of the $Fe_{73.5}Si_{13}B_{11}Cr_1C_{1.5}$ powder with −60 μm particle size (10 K/min heating rate).

Table 2
Characteristic temperatures from the DSC curves of the three kinds of powder.

Powder	T_{x1} (K)	T_{p1} (K)
GA power	817.7	826.9
WA powder	820.9	826.4
CA powder	824.3	831

heating temperature continually rising.

As seen in Fig. 8, no obvious peak appears in the XRD patterns of the three kinds of powders annealed at 693 K, 743 K, and 793 K below T_{x1} in nitrogen for 1 h, which indicates that not much crystallization took place in any powder. When an amorphous alloy is annealed at a temperature below the first crystallization onset temperature T_{x1}, structural relaxation occurs, and the atoms rearrange from a high-energy amorphous state to a low-energy crystal state. For the powder, the internal stress generated during atomization was relieved. After the powder was annealed at 843 K, which is above T_{x1}, sharp peaks appeared in the XRD pattern, and peaks location and intensity conformed to ICDD card number 03-065-9130, indicating the precipitation of the α-Fe(Si) crystalline phase.

Fig. 9 shows hysteresis loops and the partial enlarged detail around zero of the annealed powder with −60 μm particle size. The magnetic polarization intensity J_s of the WA powder, CA powder and GA powder was 1.07 T, 1.09 T, and 1.12 T, and the coercivity H_c was 151.7 A/m, 156 A/m, and 413.8 A/m, respectively. WA and CA powders are almost amorphous, while GA powder generates some α-Fe(Si) grains. The J_s of powder can be expressed as following:

$$J_s = J_s^{cry} V_{cry} + J_s^{am}(1 - V_{cry}) \quad (2)$$

Here, J_s^{cry} and J_s^{am} are the saturation magnetic polarization intensity of crystalline and amorphous phases, and V_{cry} is the volume fraction of the crystal phase. Because the amorphous phase contains metalloid elements such as P and B, its J_s^{am} is not generally greater than 1.5 T, while the J_s^{cry} of crystalline phase α-Fe(Si) can reaches 2.1 T. Therefore, when α-Fe(Si) crystal phase precipitates in the GA powder, J_s will rise up.

H_c of soft magnetic materials is proportional to the magnetocrystalline anisotropy constant K_1 and internal stress and is related to irreversible magnetic domain displacement and domain rotation during demagnetization [40]. The existence of α-Fe(Si) nanograins with a preferential orientation inside the GA powder increases the magnetocrystalline anisotropy of the powder. The higher cooling rate of the WA powder leads to higher internal stresses. In a low magnetic field, domain motion is hindered by magnetocrystalline anisotropy more than internal stress. Therefore, despite higher internal stress in the WA powder, the coercivity of the WA powder is lower than the GA powder. In addition, the grain boundaries of disorderly distributed grains in GA powder pin domain walls and impede the magnetic domain movement, which further increases H_c. The microstructure and phase state are similar in the CA and WA powder, and H_c is nearly equal as well.

3.2. Evaluation of powder application

To evaluate the application of $Fe_{73.5}Si_{13}B_{11}Cr_1C_{1.5}$ (at%) atomization powder in soft magnetic composites, toroidal magnetic powder cores were fabricated using the same process. Fig. 10 shows the variation in the effective permeability μ_e with increasing annealing temperature. The effective permeability μ_e of the GA, CA and WA magnetic powder cores annealed at 423 K is respectively 19.2, 19.7, and 20.4 and increases gradually with annealing temperature to the maximum values of 25.8, 26.9, and 29.7 after annealing at 793 K. Subsequently, μ_e drops sharply at the annealing temperature of 843 K.

The magnetization process is affected by many factors. The magnetization mechanism includes domain wall displacement and domain rotation process. The resistance of domain wall displacement comes from internal stress and impurities, while the resistance of domain rotation is mainly affected by magnetocrystalline anisotropy, internal stress and demagnetization field energy. The initial permeability μ_i (or initial susceptibility χ_i) is proportional to J_s^2 and inversely proportional to the saturation magnetostriction λ_s, internal stress σ, magnetocrystalline anisotropy constant K_1 and impurity concentration β inside the material.

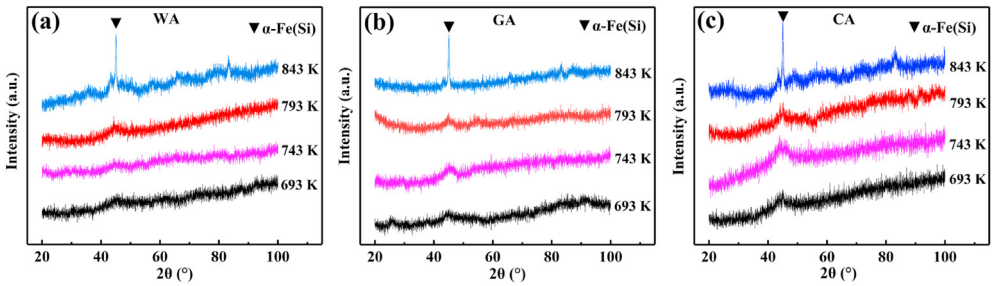

Fig. 8. XRD patterns of the $Fe_{73.5}Si_{13}B_{11}Cr_1C_{1.5}$ powder with −60 μm particle size annealed at different temperatures in nitrogen for 1 h: (a) WA, (b) GA and (c) CA.

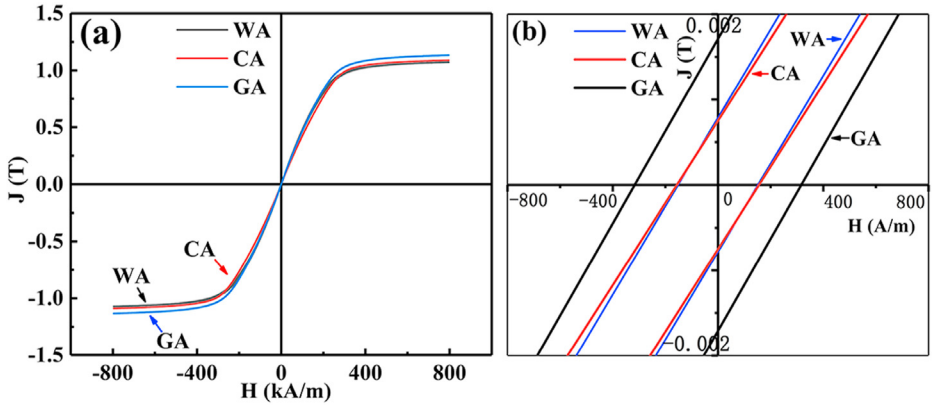

Fig. 9. Hysteresis loops of the unannealed $Fe_{73.5}Si_{13}B_{11}Cr_1C_{1.5}$ powder with −60 μm particle size: (a) Hysteresis loops and (b) Partially enlarged details of the loops.

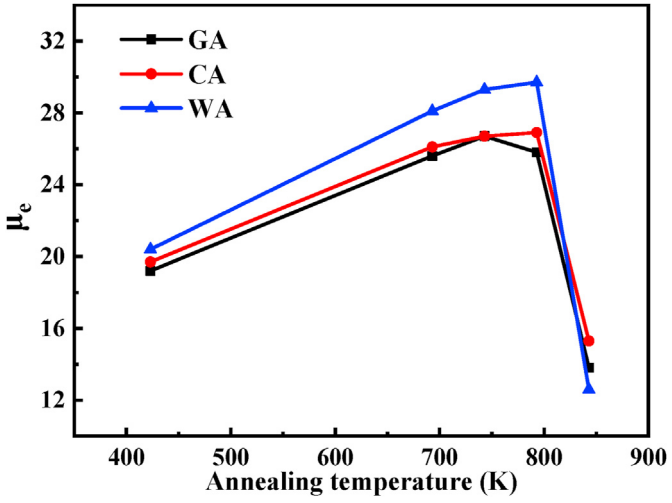

Fig. 10. Effective permeability μe of magnetic powder cores vs. annealing temperature.

As seen from Fig. 8, when the powder was annealed below 793 K, no obvious crystallization occurred, but internal stress generated during atomization and core formation was relieved, thereby decreasing the magnetoelastic energy and enabling the magnetic domains to move more easily, which tended to increase μ_e. When the magnetic powder cores were annealed at 843 K above T_{x1}, crystallization occurred, and α-Fe(Si) grains precipitated, not only increasing the magnetocrystalline anisotropy but also generating new grain boundaries, which hindered domain walls motion and magnetization, so μ_e began to degrade.

$$\mu_e = 1 + \frac{4\pi \times (\mu_i - 1)}{4\pi + N(\mu_i - 1)}\theta_i \quad (3)$$

Under the same fabricating conditions, μ_e of the magnetic powder cores changes from high to low as WA > CA > GA. For soft magnetic composites, magnetic charges aggregate on the surface of the metal soft magnetic powder, resulting in a large demagnetization field inside the powder. Note that μ_e can be expressed as in Refs. [41].

Here, θ_i is the volume percentage of a magnetic phase, μ_i is the permeability of the phase, and N is the demagnetization factor. Thus, μ_e inversely depends on the demagnetization factor N of the metal powder. The WA powder has irregular particles, resulting in a small demagnetization factor and a larger contact area between the particles after pressing, so for the same binder (nonmagnetic phase) content, μ_e of the WA magnetic powder cores is higher than other powders. Owing to point contact between the spherical powder particles in the GA and CA powders and the resulting large demagnetization factor, a relatively high demagnetization field exists inside the magnetic powder cores, so μ_e is lower for these cores than for the WA magnetic powder cores. Furthermore, μ_e of the CA magnetic powder cores is slightly higher than the GA cores. Because the cooling rate of the GA powder is lower than the CA powder, α-Fe(Si) nanograins with a preferential orientation arise inside the GA powder, which leads to easier crystallization upon annealing and a higher magnetocrystalline anisotropy. As a result, it is more difficult to magnetize the GA powder than the CA powder.

Magnetic powder cores are usually used under both direct current (DC) and alternating current (AC) existing in a circuit, which requires a suitable DC bias or DC superposition characteristic. That is, in the superimposed DC magnetic field, the decrease in permeability is as low as possible. Under this condition, the permeability is called the incremental permeability [42]:

$$\mu_{\Delta} = \frac{1}{\mu_0}\frac{\Delta B}{\Delta H} \tag{4}$$

Here, ΔH is the peak value of the alternating magnetic field intensity, ΔB is the peak value of the corresponding magnetic induction intensity, and μ_0 is the vacuum permeability. When the alternating magnetic field intensity approaches zero, the limit value of incremental permeability is defined as the reversible permeability

$$\mu_{rev} = \lim_{\Delta H \to 0} \mu_{\Delta} \tag{5}$$

Fig. 11 is a schematic diagram of the incremental permeability [35]. Under a certain DC magnetic field, an AC magnetic field with an amplitude of ΔH/2 is superimposed on the magnetization curve to form a small elliptical hysteresis loop at one point on the magnetization curve. As the DC magnetic field increases, the magnetic induction intensity gradually reaches the saturation magnetic induction intensity B_s, and magnetization becomes increasingly difficult. The slope of the small hysteresis loop also gradually tilts toward the H axis, thus decreasing the incremental permeability. The tendency of saturation in the magnetic powder cores is the reason for the decrease in the incremental permeability. Delaying this saturation tendency is a way to improve the DC bias.

The decreasing trend in the incremental permeability with an increasing DC magnetic field is related to the material, shape, and particle size of the powder and the preparation process of the magnetic powder core. With a lower stress and fewer inclusions and defects inside the material, the reversible magnetization stage is prolonged, which can delay reaching saturation. The variation in the relative permeability of cores annealed at 793 K with an increasing DC magnetic field is shown in Fig. 12. The permeability of all three kinds of magnetic powder cores decreases with the field strength. Here, the permeability of the WA magnetic powder cores drops the most, followed by the GA cores permeability and finally the CA cores permeability. Under a DC magnetic field of 7.96 kA/m, the relative permeability of the cores is 83.3%, 80.1%, and 75.9%, respectively, which indicates that the CA magnetic powder cores have the best DC bias performance. Because of the identical composition, nearly identical particle size, and identical preparation process for the three cores, the powder shape and internal state of the material are the factors primarily influencing the DC bias characteristics. As mentioned above, a demagnetization field exists between the particles, so the actual magnetic field intensity inside the material is lower than the applied magnetic field. The actual magnetic field intensity between spherical powder particles with a high demagnetization field is lower than the irregular powder with a low demagnetization field, so the CA and GA magnetic powder cores tend to saturate more slowly than the WA magnetic powder cores. In addition, more crystalline phases exist in the GA powder, which makes reversible magnetization more difficult than for the CA powder, resulting in a faster decrease in the incremental permeability for the GA powder than for the CA powder.

To save energy, reduce the operating temperature of magnetic powder cores and prolong the service life of electronic devices, the energy loss of the magnetic powder cores should be minimized. The core loss consists of three parts: the hysteresis loss, residual loss, and eddy current loss, wherein the residual loss comes from magnetization relaxation and resonance of the domain walls, which is only important under high frequencies and weak magnetic fields. By omitting this residual loss, the total loss can be expressed in Ref. [43]:

$$P_{cv} = P_h + P_e = K_h B_m^n f + K_e B_m^2 f^2 \tag{6}$$

Here, P_{cv} is the total core loss, K_h is the hysteresis loss coefficient, K_e is the core loss coefficient, B_m is the magnetic field amplitude, f is the frequency, and n is a constant.

The hysteresis loss and eddy current loss have different generation mechanisms, so it is necessary to separate them within the total loss. At constant B_m, dividing both sides of Eq. (6) by f yields:

$$\frac{P_{cv}}{f} = K_h B_m^n + K_e B_m^2 f = a + bf \tag{7}$$

P_{cv}/f is linearly related to f. Measuring the total loss at different frequencies and linearly fitting data points, one can obtain the hysteresis loss and eddy current loss as

$$P_h = af \tag{8}$$

$$P_e = bf^2 \tag{9}$$

Fig. 13 shows a comparison between the measured total loss and the sum of the calculated hysteresis loss and eddy current of

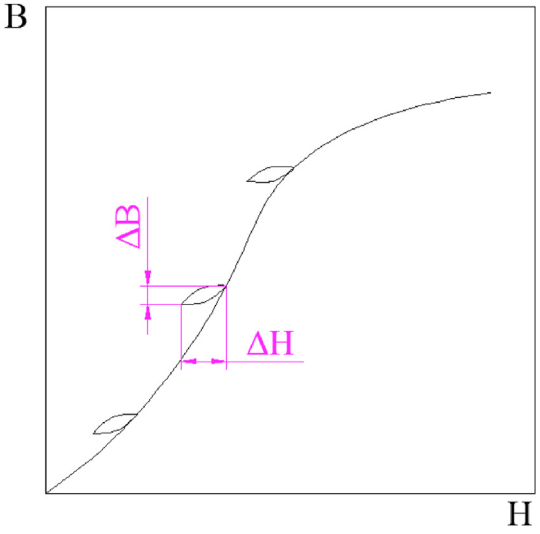

Fig. 11. Schematic diagram of incremental permeability.

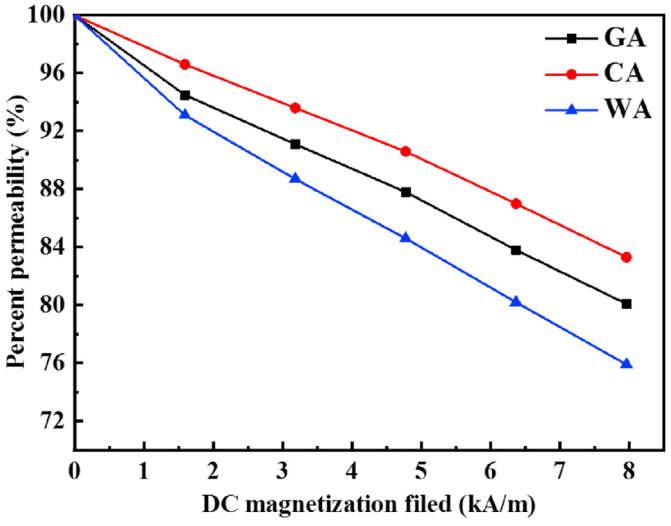

Fig. 12. DC bias of the magnetic powder cores annealed at 793 K.

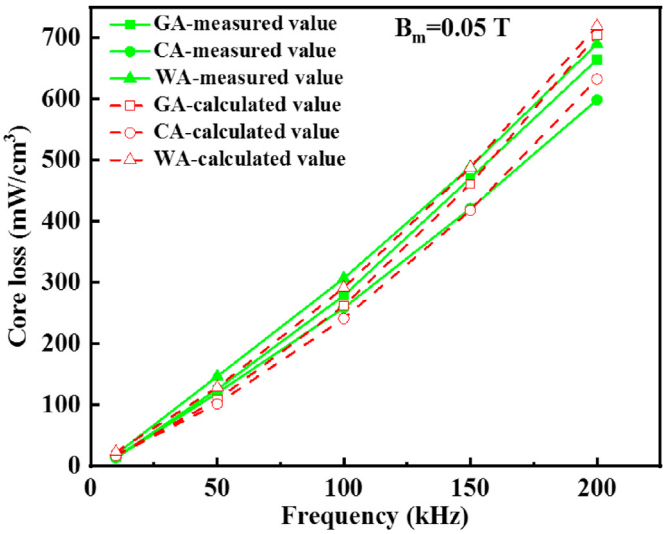

Fig. 13. Core loss comparison between the measured and calculated values of magnetic powder cores annealed at 793 K (B_m = 0.05 T).

magnetic powder cores annealed at 793 K according to Eqs. (7)–(9). The relative error is larger at low frequencies (10 kHz, 50 kHz), and the maximum is 27%. However, the relative error is less at high frequencies (100 kHz, 150 kHz, 200 kHz), and the maximum is 7%. The authors find the calculated results acceptable. Fig. 14 shows the measured loss values of cores annealed at different temperatures under f = 100 kHz and B_m = 0.05 T. The total core loss of GA, CA and WA cores annealed at 423 K is 1083 mW/cm^3, 991 mW/cm^3, and 1291 mW/cm^3, respectively. With the rising annealing temperature, the core loss decreases gradually to a minimum of 278 mW/cm^3, 258 mW/cm^3, and 306 mW/cm^3, respectively, for 793 K annealing. When the annealing temperature is increased further to 843 K, the corresponding core loss increases sharply to 1375 mW/cm^3, 1278 mW/cm^3, and 1509 mW/cm^3.

Figs. 15 and 16 show the calculated hysteresis loss and eddy current loss, respectively, both of which exhibit a consistent change trend with the total loss. Under the same test conditions, the hysteresis loss is larger than the eddy current loss. With the annealing temperature rising, the stress caused in the powder during the

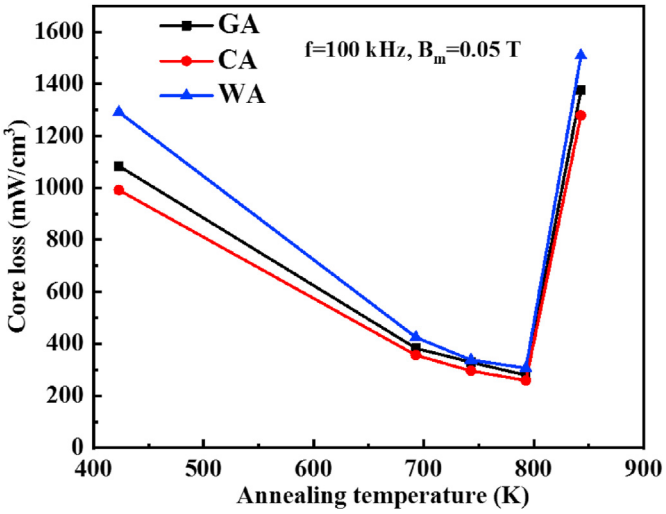

Fig. 14. Measured total core loss of magnetic powder cores annealed at different temperatures (f = 100 kHz, B_m = 0.05 T).

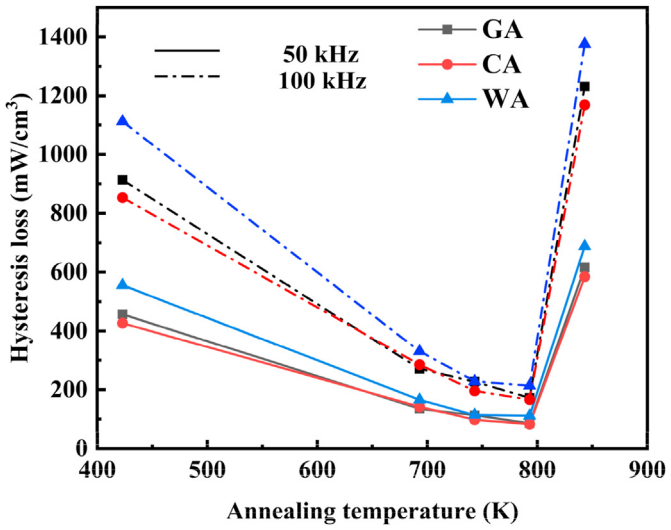

Fig. 15. Hysteresis loss of magnetic powder cores annealed at different temperatures (f = 50 kHz, 100 kHz; B_m = 0.05 T).

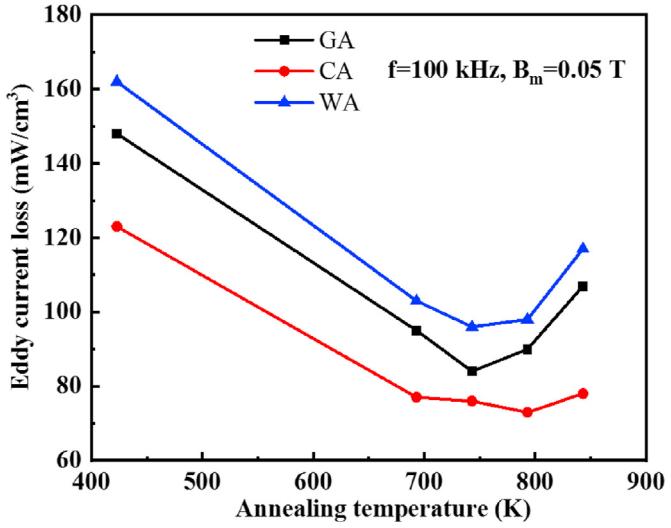

Fig. 16. Eddy loss of magnetic powder cores annealed at different temperatures (f = 100 kHz, B_m = 0.05 T).

atomization process and core fabrication decreases gradually, so the obstacles to domain wall movement decrease. After annealing at 793 K, the hysteresis loss of the cores decreases to their minimum values: 213 mW/cm^3, 172 mW/cm^3, and 166 mW/cm^3 for the WA, GA and CA magnetic powder cores, respectively. When annealed at 843 K above the first crystallization temperature T_{x1}, all three powders are substantially crystallized, and the generated α-Fe(Si) nanograins increase the magnetocrystalline anisotropy of the material, resulting in a great increase in the hysteresis loss.

The eddy current loss also first decreases and then increases with the annealing temperature. In the cores annealed at 793 K, the eddy current loss is the lowest: 98 mW/cm^3, 90 mW/cm^3, and 73 mW/cm^3 for the WA, GA and CA cores, respectively. When the annealing temperature rises to 843 K, the eddy current loss also increases, but the amplitude is smaller than the hysteresis loss. The eddy current loss is directly related to the resistivity of the material. No long-range order exists in an amorphous alloy, but there is a short-range order. Electrons scattered by disordered atoms and vacancy defects predominantly determine the resistivity at room

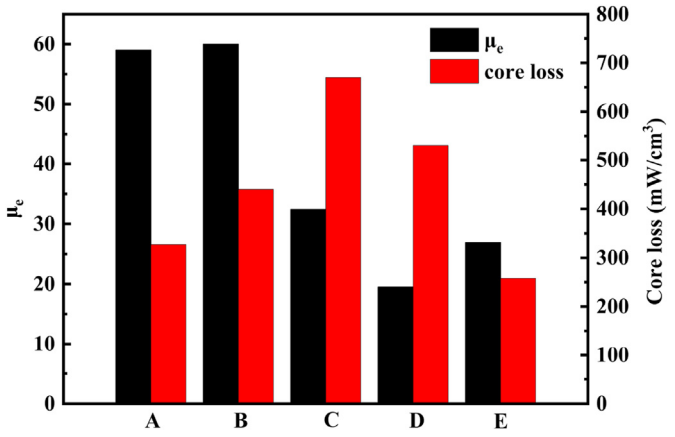

Fig. 17. Comparison of μ_e and core loss of crystalline and amorphous powder cores: (A) $Fe_{50}Ni_{50}$ (wt%), (B) $Fe_{93.5}Si_{6.5}$ (wt%), (C) $Fe_{89.5}Si_5Cr_{5.5}$ (wt%), (D) $Fe_{78}Si_9B_{13}$ (at%), and (E) $Fe_{73.5}Si_{13}B_{11}Cr_1C_{1.5}$ (at%).

temperature. During the annealing process, amorphous alloys undergo a relaxation process and transition to more stable amorphous or crystalline states, thereby changing the structural and chemical short-range ordering. At lower annealing temperatures, atoms with smaller diameters such as B and Si move short distances to create vacancies and disrupt this short-range order, consequently increasing the resistivity. With the annealing temperature rising, the completion of atomic rearrangement tends to increase the ordering until crystallization begins and grains form; as a result, electron scattering decreases, the alloy conductivity increases, and the resistivity decreases [44]. As a result of this change in the resistivity, the eddy current loss first decreases and then increases.

Figs. 14–16 also show that at the same annealing temperature, the total loss of the WA powder cores is the highest, followed by the GA powder cores and then by the CA cores. The CA powder particles have the most spherical shapes and the smoothest surfaces, which is beneficial for insulation coating, while the protrusions on the surfaces of the irregular particles in the WA powder can easily puncture the insulating layer when cores are fabricated, causing eddy current to pass between particles and a resulting higher loss.

Both magnetocrystalline anisotropy and stress anisotropy hinder domain movement; although there is no macroscale magnetocrystalline anisotropy in amorphous alloys, there is stress anisotropy. WA has the fastest cooling rate in the three kinds of atomization processes, which results in a larger internal stress inside the powder particles, so during repeated magnetization, the hysteresis loss is higher than the other two processes. In contrast, GA and CA have lower cooling rates, resulting in less internal stress and a lower hysteresis loss. Furthermore, because a nanocrystalline α-Fe(Si) phase forms inside the GA particles, the corresponding magnetocrystalline anisotropy is higher than the CA powder, so the hysteresis loss of the CA powder is higher than the GA powder.

In order to compare the properties of $Fe_{73.5}Si_{13}B_{11}Cr_1C_{1.5}$ (at%) powder with other soft magnetic powders, $Fe_{50}Ni_{50}$ (wt%), $Fe_{93.5}Si_{6.5}$ (wt%), and $Fe_{89.5}Si_5Cr_{5.5}$ (wt%) crystalline powder cores, and $Fe_{78}Si_9B_{13}$ (at%) amorphous powder cores were fabricated with the same forming pressure and binder content. As seen in Fig. 17, although μ_e of the $Fe_{73.5}Si_{13}B_{11}Cr_1C_{1.5}$ (at%) powder cores is lower than crystalline powder cores, the core loss is the lowest among these alloys powder, which indicates that the CA powder is suitable for high-frequency applications.

4. Conclusions

Aiming to obtain the spherical amorphous powder, the authors developed CA technology, prepared $Fe_{73.5}Si_{13}B_{11}Cr_1C_{1.5}$ (at%) amorphous powder by the WA, GA and CA processes and corresponding magnetic powder cores, and compared the properties of the resulting preparations. The results indicate that:

- The cooling rate of metal droplets during GA is the lowest among the three techniques, and α-Fe(Si) nanograins with preferred orientation precipitate inside the −60 μm powder. The cooling rate of the metal droplets during WA and CA is higher than that of GA, and the −60 μm powder is entirely amorphous. H_c of WA, CA and GA is 151.7 A/m, 156 A/m, and 413.8 A/m, respectively. The WA powder contains some irregular particles, but the CA powder particles are almost spherical.
- When the magnetic powder cores are annealed at temperatures below T_{x1}, the effective permeability μ_e increases and the core loss decreases with temperature. When the temperature exceeds T_{x1}, μ_e decreases rapidly, and the core loss increases sharply. When the magnetic powder cores are annealed at 793 K, μ_e reaches the maximum whereas the core loss reaches the minimum. Furthermore, μ_e of the WA, GA and CA magnetic powder cores is 29.7, 25.8, and 26.9, respectively, and the corresponding total core loss is 306 mW/cm^3, 278 mW/cm^3, and 258 mW/cm^3, wherein the hysteresis loss accounts for the majority of the total core loss.
- The CA magnetic powder cores have the best DC bias characteristic of the three types. The relative permeability is 83.3% at an applied DC magnetic field of 7.96 kA/m.

Data availability

The raw/processed data required to reproduce these findings cannot be shared at this time as the data also forms part of an ongoing study.

CRediT authorship contribution statement

Tongchun Zhao: Methodology, Validation, Investigation, Resources, Writing - original draft, Visualization. **Cunguang Chen:** Conceptualization, Methodology, Validation, Writing - review & editing. **XiaoJie Wu:** Resources, Formal analysis, Data curation. **Chenzeng Zhang:** Resources, Formal analysis, Data curation. **Alex A. Volinsky:** Writing - review & editing. **Junjie Hao:** Methodology, Resources, Funding acquisition.

Declaration of competing interest

The authors declare that they have no known competing financial interests or personal relationships that could have appeared to influence the work reported in this paper.

Acknowledgements

This work was supported by the State Key Lab for Advanced Metals and Materials of China (2019-Z10), and the Fundamental Research Funds for the Central Universities (FRF-GF-19-012AZ).

References

[1] K.J. Sunday, M.L. Taheri, Soft magnetic composites: recent advancements in the technology, MPR 72 (2017) 425–429.
[2] Y.P. Yamada, E.A. Périgo, Y. de Hazan, S. Nakahara, Permeability of hybrid soft magnetic composites, Acta Mater. 59 (2011) 4291–4302.
[3] Z.G. Luo, X.A. Fan, W.T. Hu, F. Luo, G.Q. Li, Y.W. Li, J. Wang, X. Liu, Effect of sintering temperature on microstructure and magnetic properties for Fe-Si soft magnetic composites prepared by water oxidation combined with spark plasma sintering, J. Magn. Magn Mater. 491 (2019) 165615.
[4] W.C. Li, Y.Y. Pu, Y. Ying, Y. Kang, J. Yu, J.W. Zheng, L. Qiao, J. Li, S.L. Che, Magnetic properties and related mechanisms of iron-based soft magnetic composites with high thermal stability in situ composite ferrite coating, J. Alloys Compd. 829 (2020) 154533.
[5] J.G. Yeo, D.H. Kim, Y.J. Choi, B.W. Lee, Improving power-inductor performance by mixing sub-micro Fe powder with amorphous soft magnetic composites, J. Electron. Mater. 48 (2019) 6018–6023.
[6] Q.S. Meng, F.Y. Yang, X.Y. Wu, T.T. Xu, M.M. Zhou, W.W. Guan, H.L. Su, Y. Han, Y.W. Du, Magnetic spectra of soft magnetic composites based on Fe-Si-Cr-B amorphous and carbonyl-iron powders, J. Supercond. Nov. Magnetism 32 (2019) 2987–2994.
[7] B. Zhou, Q. Chi, Y.Q. Dong, L. Liu, Y.Q. Zhang, L. Chang, Y. Pan, A.N. He, J.W. Li, X.N. Wang, Effects of annealing on the magnetic properties of Fe-based amorphous powder cores with inorganic-organic hybrid insulating layer, J. Magn. Magn Mater. 494 (2020) 165827.
[8] T. Suzuki, P. Sharma, A. Makino, Extending the operational frequency range of high B_s - FeSiBP amorphous alloy to GHz by coating the powder surface with silicon oxide, J. Magn. Magn Mater. 491 (2019) 165641.
[9] D.N. Chen, K.L. Li, H.Y. Yu, J.L. Zuo, X. Chen, B.C. Guo, G.Z. Han, Z.W. Liu, Effects of secondary particle size distribution on the magnetic properties of carbonyl iron powder cores, J. Magn. Magn Mater. 497 (2020) 166062.
[10] J. Füzerová, J. Füzer, P. Kollár, R. Bureš, M. Fáberová, Complex permeability and core loss of soft magnetic Fe-based nanocrystalline powder cores, J. Magn. Magn Mater. 345 (2013) 77–81.
[11] K.J. Sunday, F.G. Hanejko, M.L. Taheri, Magnetic and microstructural properties of Fe_3O_4-coated Fe powder soft magnetic composites, J. Magn. Magn Mater. 423 (2017) 164–170.
[12] P. Kollár, P. Slovenský, D. Olekšáková, M. Jakubčin, Z. Birčáková, J. Füzera, R. Bureš, M. Fáberová, Preparation and magnetic properties of NiFeMo powdered compacts of powder elements with smoothed surfaces, J. Magn. Magn Mater. 494 (2020) 165770.
[13] W. Xu, C. Wu, M. Yan, Preparation of Fe-Si-Ni soft magnetic composites with excellent high-frequency properties, J. Magn. Magn Mater. 381 (2015) 116–119.
[14] L. Zhu, H. Zheng, S.S. Jiang, Y.G. Wang, Modulating the crystallization process of $Fe_{82}B_{12}C_6$ amorphous alloy via rapid annealing, J. Alloys Compd. 785 (2019) 328–334.
[15] L. Zhu, S.N. Liu, S. Lan, Y.M. Xu, C. Li, H. Zheng, S.S. Jiang, J.R. Men, X.-L. Wang, F.M. Pan, Y.G. Wang, Structural rearrangement at medium-range and its effects on the magnetic properties and crystallization behaviors of a Fe-based amorphous alloy, J. Alloys Compd. 823 (2020) 153911.
[16] L. Zhu, S.N. Liu, S. Lan, Y.M. Xu, C. Li, H. Zheng, S.S. Jiang, J.R. Men, X.L. Wang, F.M. Pan, Y.G. Wang, Structural rearrangement at medium-range and its effects on the magnetic properties and crystallization behaviors of a Fe-based amorphous alloy, J. Alloys Compd. 823 (2020) 153911.
[17] Z.C. Li, Y.Q. Dong, F.S. Li, C.T. Chang, X.M. Wang, R.W. Li, Fe78Si9B13 amorphous powder core with improved magnetic properties, J. Mater. Sci. Mater. Electron. 28 (2017) 1180–1185.
[18] F.L. Kong, Y. Han, X.H. Wang, SENNTIX-type amorphous alloys with high Bs and improved corrosion resistance, J. Alloys Compd. 707 (2017) 195–198.
[19] H. Takafumi, B. Teruo, Ternary Fe-B-C and quaternary Fe-B-C-Si amorphous alloys with glass transition and high magnetization, J. Alloys Compd. 707 (2017) 82–86.
[20] H.B. Sun, Z.L. Guo, Z.K. Liang, W.H. Chen, Q.T. Zeng, C. Wang, Enhancements of preparation efficiency and magnetic properties for Fe-based amorphous magnetic flake powder cores upon the adoption of a novel double-paralleled slits nozzle, J. Magn. Magn Mater. 500 (2020) 166358.
[21] X.Y. Wang, Z.C. Lu, C.W. Lu, G.M. Li, D.R. Li, Magnetic properties of Fe(Si)BC amorphous alloy powder cores using mechanical-crushed powder, J. Iron Steel Res. Int. 21 (2014) 1055–1058.
[22] B.V. Neamt, T.F. Marinca, I. Chicinas, O. Isnard, Structural, magnetic and thermal characterization of amorphous FINEMET powders prepared by wet mechanical alloying, J. Alloys Compd. 626 (2015) 49–55.
[23] X.L. Li, Y.Y. Wu, S.T. Yang, X.J. Cha, P.C. Shao, L. Wang, Preparation and degradation property of magnetic FePBCSi amorphous alloy powder, J. Non-Cryst. Solids 503–504 (2019) 284–287.
[24] Y.Y. Zheng, Y.G. Wang, G.T. Xia, Amorphous soft magnetic composite-cores with various orientations of the powder-flakes, J. Magn. Magn Mater. 396 (2015) 97–101.
[25] E.J. Lavernia, T.S. Srivatsan, The rapid solidification processing of materials: science, principles, technology, advances, and applications, J. Mater. Sci. 45 (2010) 287–325.
[26] C.T. Chang, Y.Q. Dong, M. Liu, H.Q. Guo, Q. Xiao, Y.F. Zhang, Low core loss combined with high permeability for Fe-based amorphous powder cores produced by gas atomization powders, J. Alloys Compd. 766 (2018) 959–963.
[27] Kenny L. Alvarez, H.A. Baghbaderani, J.M. Martín, N. Burgos, M. Ipatov, Z. Pavlovic, P. McCloskey, A. Masood, J. Gonzalez, Novel Fe-based amorphous and nanocrystalline powder cores for high frequency power conversion, J. Magn. Magn Mater. 501 (2020) 166457.
[28] Y. Liu, S. Niu, F. Li, Y.H. Zhu, Preparation of amorphous Fe-based magnetic powder by water atomization, Powder Technol. 213 (2011) 36–40.
[29] J.J. Guo, Y.Q. Dong, Q.K. Man, Q. Li, C.T. Chang, X.M. Wang, R.W. Li, Fabrication of FeSiBPNb amorphous powder cores with high DC-bias and excellent soft magnetic properties, J. Magn. Magn Mater. 401 (2016) 432–435.
[30] I. Otsuka, K. Wada, Y. Maeta, T. Kadomura, M. Yagi, Magnetic properties of Fe-based amorphous powders with high-saturation induction produced by spinning water atomization process (SWAP), IEEE Trans. Magn. 44 (2008) 3891–3894.
[31] N. Ciftci, N. Yodoshi, S. Armstrong, Processing soft ferromagnetic metallic glasses: on novel cooling strategies in gas atomization, hydrogen enhancement, and consolidation, J. Mater. Sci. Technol. 59 (2020) 26–36.
[32] T. Hibino, T. Bitoh, Ternary Fe-B-C and Quaternary Fe-B-C-Si amorphous alloys with glass, transition and high magnetization, J. Alloys Compd. 707 (2017) 82–86.
[33] S.L. Wang, H.X. Li, X.F. Zhang, S. Yi, Effects of Cr contents in Fe-based bulk metallic glasses on the glass forming ability and the corrosion resistance, Mater. Chem. Phys. 113 (2009) 878–883.
[34] D.D. Xu, L. Zhou, Q.Q. Wang, J. Zhou, W.M. Yang, C.C. Yuan, L. Xue, X.D. Fan, L.Q. Ma, B.L. Shen, Effects of Cr addition on thermal stability, soft magnetic properties and corrosion resistance of FeSiB amorphous alloys, Corrosion Sci. 138 (2018) 20–27.
[35] S.F. Chen, C.Y. Chen, C.S. Cheng, Passivation layer for the magnetic property enhancement of $Fe_{72.8}Si_{11.2}B_{10.8}Cr_{2.3}C_{2.9}$ amorphous powder, J. Alloys Compd. 644 (2015) 17–24.
[36] H.B. Sun, C. Wang, J.H. Wang, M.G. Yu, Z.L. Guo, Fe-based amorphous powder cores with low core loss and high permeability fabricated using the core-shell structured magnetic flaky powders, J. Magn. Magn Mater. 502 (2020) 166548.
[37] V.V. Sobolev, J.M. Guilemany, A.J. Martin, Powder particle structure formation during solidification in the process of metal atomization, J. Mater. Process. Technol. 54 (1995) 249–260.
[38] D. Beckers, N. Ellendt, U. Fritsching, V. Uhlenwinkel, Impact of process flow conditions on particle morphology in metal powder production via gas atomization, Adv. Powder Technol. 31 (2020) 300–311.
[39] M. Boisvert, D. Christopherson, P. Beaulieu, G. L'Espérance, Treatment of ferrous melts for the improvement of the sphericity of water atomized powders, Mater. Des. 116 (2017) 644–655.
[40] K.H.J. Buschow, F.R. de Boer, Physics of Magnetism and Magnetic Materials, Springer-Verlag New York Inc, New York, 2013.
[41] Y.Y. Zheng, Y.G. Wang, Amorphous soft magnetic composite-cores with various orientations of the powder-flakes, J. Magn. Magn Mater. 396 (2015) 97–101.
[42] V.T. Zaspalis, V. Tsakaloudi, M. Kolenbrander, The effect of dopants on the incremental permeability of MnZn-Ferrites, J. Magn. Magn Mater. 313 (2007) 29–36.
[43] Y. Zhang, P. Sharma, A. Makino, Sintered powder cores of high B_s and low coreloss $Fe_{84.3}Si_4B_8P_3Cu_{0.7}$ nano-crystalline alloy, AIP Adv. 3 (2013), 062118.
[44] I. Mat'ko, E. Illekovfi, P. Svec, P. Duhaj, Crystallization characteristics in the Fe-Si-B glassy ribbon system, Mater. Sci. Eng. A 225 (1997) 145–152.